


ORIGINAL RESEARCH

Open Access



^{18}F -FDG PET and DCE kinetic modeling and their correlations in primary NSCLC: first voxel-wise correlative analysis of human simultaneous $[^{18}\text{F}]$ FDG PET-MRI data

Florent L. Besson^{1,2,3*} , Brice Fernandez⁴, Sylvain Faure⁵, Olaf Mercier⁶, Andrei Seferian^{7,8}, Xavier Mignard⁷, Sacha Mussot⁶, Cecile le Pechoux⁹, Caroline Caramella¹⁰, Angela Botticella⁹, Antonin Levy⁹, Florence Parent^{7,8}, Sophie Bulifon^{7,8}, David Montani^{7,8}, Delphine Mitilian⁶, Elie Fadel⁶, David Planchard¹¹, Benjamin Besse¹¹, Maria-Rosa Ghigna-Bellinzoni¹², Claude Comtat^{1,3}, Vincent Lebon^{1,3} and Emmanuel Durand^{1,2,3}

Abstract

Objectives: To decipher the correlations between PET and DCE kinetic parameters in non-small-cell lung cancer (NSCLC), by using voxel-wise analysis of dynamic simultaneous $[^{18}\text{F}]$ FDG PET-MRI.

Material and methods: Fourteen treatment-naïve patients with biopsy-proven NSCLC prospectively underwent a 1-h dynamic $[^{18}\text{F}]$ FDG thoracic PET-MRI scan including DCE. The PET and DCE data were normalized to their corresponding T_1 -weighted MR morphological space, and tumors were masked semi-automatically. Voxel-wise parametric maps of PET and DCE kinetic parameters were computed by fitting the dynamic PET and DCE tumor data to the Sokoloff and Extended Tofts models respectively, by using in-house developed procedures. Curve-fitting errors were assessed by computing the relative root mean square error (rRMSE) of the estimated PET and DCE signals at the voxel level. For each tumor, Spearman correlation coefficients (r_s) between all the pairs of PET and DCE kinetic parameters were estimated on a voxel-wise basis, along with their respective bootstrapped 95% confidence intervals ($n = 1000$ iterations).

Results: Curve-fitting metrics provided fit errors under 20% for almost 90% of the PET voxels (median rRMSE = 10.3, interquartile ranges IQR = 8.1; 14.3), whereas 73.3% of the DCE voxels showed fit errors under 45% (median rRMSE = 31.8%, IQR = 22.4; 46.6). The PET-PET, DCE-DCE, and PET-DCE voxel-wise correlations varied according to individual tumor behaviors. Beyond this wide variability, the PET-PET and DCE-DCE correlations were mainly high (absolute r_s values > 0.7), whereas the PET-DCE correlations were mainly low to moderate (absolute r_s values < 0.7). Half the tumors showed a hypometabolism with low perfused/vascularized profile, a hallmark of hypoxia, and tumor aggressiveness.

(Continued on next page)

* Correspondence: florent.besson@aphp.fr

¹Université Paris-Saclay, CEA, CNRS, Inserm, BioMAPs, 91401 Orsay, France

²Department of Biophysics and Nuclear Medicine-Molecular Imaging, Hôpitaux Universitaires Paris-Saclay, Assistance Publique-Hôpitaux de Paris, CHU Bicêtre, 94270 Le Kremlin-Bicêtre, France

Full list of author information is available at the end of the article



© The Author(s). 2020 **Open Access** This article is licensed under a Creative Commons Attribution 4.0 International License, which permits use, sharing, adaptation, distribution and reproduction in any medium or format, as long as you give appropriate credit to the original author(s) and the source, provide a link to the Creative Commons licence, and indicate if changes were made. The images or other third party material in this article are included in the article's Creative Commons licence, unless indicated otherwise in a credit line to the material. If material is not included in the article's Creative Commons licence and your intended use is not permitted by statutory regulation or exceeds the permitted use, you will need to obtain permission directly from the copyright holder. To view a copy of this licence, visit <http://creativecommons.org/licenses/by/4.0/>.

(Continued from previous page)

Conclusion: A dynamic “one-stop shop” procedure applied to NSCLC is technically feasible in clinical practice. PET and DCE kinetic parameters assessed simultaneously are not highly correlated in NSCLC, and these correlations showed a wide variability among tumors and patients. These results tend to suggest that PET and DCE kinetic parameters might provide complementary information. In the future, this might make PET-MRI a unique tool to characterize the individual tumor biological behavior in NSCLC.

Keywords: PET-MRI, DCE-MRI, [18F]FDG, Kinetic parameters, NSCLC, Quantification

Introduction

Positron emission tomography (PET) combined with magnetic resonance imaging (MRI) emerged a decade ago [1, 2]. Since then, substantial efforts have been made to promote its clinical use, but disappointing results compared to more cost-effective and former imaging modalities still make the positioning of PET-MRI challenging in clinical practice [3]. In the era of precision medicine, advanced multiparametric imaging offers many opportunities to better characterize the biological processes of tumors [4–6]. In contrast to standard visual or semi-quantitative imaging methods, the more advanced dynamic quantitative imaging approach allows the absolute quantification of various sophisticated biological processes, based on the pharmacokinetic modeling of tracer exchanges. PET kinetic modeling of [18F]FDG quantifies the glucose metabolic pathway in tumor cells, characterized by the related K_1 , k_2 , and k_3 PET microparameters [7]. Previous dynamic PET studies showed [18F]FDG microparameters to be surrogates of tumor aggressiveness or prognosis factors in a wide variety of malignancies [8–11], including primary non-small-cell lung cancer model (NSCLC) [12]. In magnetic resonance imaging (MRI), dynamic contrast-enhanced MRI (DCE-MRI) provides insight into the underlying tumor vascularization at the microcirculatory level, depending on the contrast agent leakage through the capillary wall. In the case of gadolinium (Gd), the K_{trans} , v_e , K_{ep} (the K_{trans} to v_e ratio), and v_p microparameters reflect the perfusion, permeability, and microvascular density properties of the tumor [13]. Previous oncological studies showed DCE microparameters to be significant predictors of response to treatment in several malignancies [14–17], including NSCLC [18].

Metabolism and vascularization are two fundamental hallmarks of cancer [19], and their relationships are of particular relevance to capture the tumor progression and responses to treatment capabilities [20]. In integrated PET-MRI, combining PET and DCE kinetic modeling may be thus of particular interest to revisit the complex relationship between these two fundamental tumor hallmarks [19, 20] at the intra-tumor regional level. In lung cancer, previous [18F]FDG PET/MRI imaging studies have been performed mainly for clinical

disease staging evaluation [21–25], SUV-ADC correlation analyses [26–29], and prognostic value [30]. To date, only a few multimodal imaging studies compared tumor metabolism assessed with PET and angiogenesis assessed with DCE in NSCLC [31–35], of which only two combined dedicated [18F]FDG PET and DCE-MRI imaging data [31, 35]. So far, a combined voxel-wise analysis of simultaneous dynamic [18F]FDG PET and DCE-MRI has never been performed at the individual tumor level.

In this study, we deciphered the correlations between [18F]FDG PET and DCE kinetic parameters at the intra-tumor level in newly diagnosed, biopsy proven NSCLC, by using a combined voxel-wise analysis of dynamic simultaneous [18F]FDG PET-MRI.

Material and methods

Patients

Between January 2018 and April 2019, a total of 14 treatment-naïve patients with biopsy proven NSCLC prospectively underwent a dynamic [18F]FDG PET-MRI for thoracic oncology purposes. The exclusion criteria were claustrophobia, metal implants, renal failure (clearance < 30 mL/min), and uncontrolled diabetes mellitus. Patient characteristics are summarized in Table 1. The local institutional review board approved this study (SHFJ Research Steering Committee, DRF/JOLIOT/SHFJ/2020/10), and all patients signed written informed consent.

PET/MRI

All the examinations were performed in the supine position on the same integrated 3 T PET-MRI scanner (Signa PET/MR, GE Healthcare, Waukesha, WI, USA). All patients fulfilled the international procedure guideline for [18F]FDG PET tumor imaging [36], having fasted for 6 h and a blood glucose level under 1.8 g/L at the time of the imaging procedure. A 1-h dynamic thoracic PET acquisition started immediately after the intravenous injection of 3–4 MBq/kg of [18F]FDG. The dynamic PET data were histogrammed into multiframe sinograms (41 frames of 12 × 10 s, 12 × 20 s, 4 × 60 s, 5 × 120 s, 8 × 300 s, respectively) to be reconstructed using an iterative algorithm (3D TOF-OSEM, 6 iterations, and

Table 1 Patients characteristics

Patient	Age	Gender	NSCLC localization	Histology	Voxels (2 mm ³)
1	82	M	Right upper lobe	Poorly differentiated NSCLC	540
2	47	M	Right upper lobe	NSCLC	1271
3	71	F	Right lower lobe	NSCLC (undifferentiated carcinoma)	799
4	67	F	Left upper lobe	NSCLC (ADK)	211
5	80	F	Left upper lobe	NSCLC (SCC)	1207
6	53	M	Right medium lobe	NSCLC (ADK)	88
7	78	F	Left upper lobe	NSCLC (ADK)	629
8	55	M	Right upper lobe	NSCLC (ADK)	318
9	63	M	Left upper lobe	NSCLC (poorly differentiated SCC)	2409
10	57	M	Left upper lobe	NSCLC (ADK)	2338
11	62	M	Right upper lobe	NSCLC (ADK)	1151
12	61	M	Right upper lobe	NSCLC (SCC)	5340
13	71	F	Right upper lobe	NSCLC (ADK)	3845
14	71	M	Right upper lobe	NSCLC (ADK)	1409

ADK adenocarcinoma, SCC squamous cell carcinoma

28 subsets with time of flight and point spread function modeling, and with random, dead time, scatter, decay, and attenuation corrections, matrix size = 256 × 256; voxel size = 2 × 2 × 2.78 mm). Simultaneously, the following MR thoracic acquisitions were performed using a thoracic phased array radiofrequency (RF) coil (GEM Coil Suite, GE Healthcare, Waukesha, WI, USA):

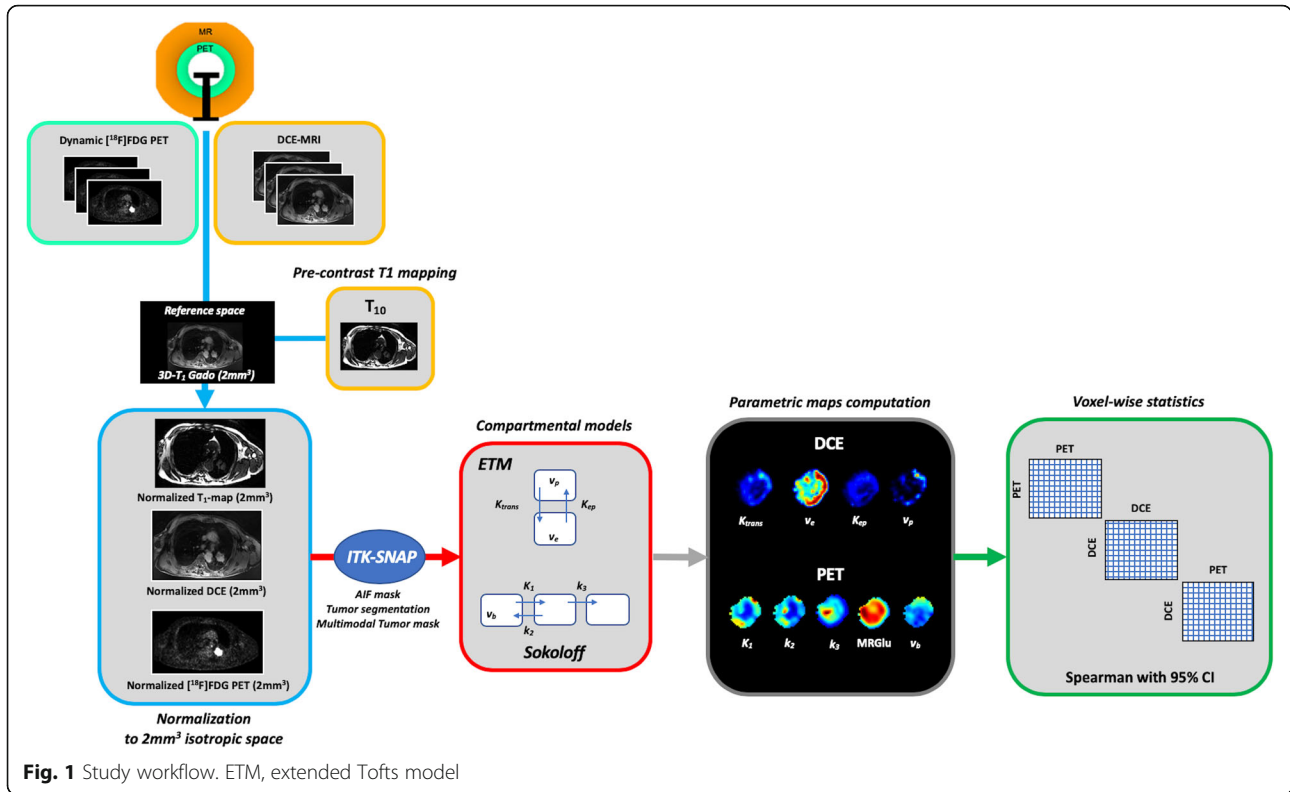
- A two-point (fat, water) axial 3D-Dixon pulse sequence (TR/TE₁/TE₂ = 4/1.1/2.2 ms, Field-Of-View (FOV): 500/500/332.8 mm, number of excitations (NEX) = 0.7, voxel size 1.95 × 1.95 × 2.6 mm) for MR-based attenuation correction.
- A PROPELLER fast recovery Fast Spin Echo sequence with respiratory triggering for T₂-weighted morphology (TR/TE = 8000/117 ms, FOV: 400/400/90 mm, NEX = 2; voxel size 1.0 × 1.0 × 6.0 mm, acceleration factor = 3).
- A 2D saturation recovery pulse sequence for pre-contrast T₁-mapping (cardiac triggered, inversion times = [136/136/136/136/818/1583/2109/2808/20000] ms, TR/TE = 2.9/1.1 ms; FOV: 420/420/30 mm, NEX = 1; voxel size 1.64 × 1.64 × 5.0 mm) [37].
- DCE acquisitions performed before, during, and after the automated injection of gadolinium contrast agent (Gd, 0.2 mmol/kg body weight, Dotarem, Guerbet GmbH, Germany; injecting rate of 2.0 mL/s by power injector) using 3D T₁-Fast Spoiled Gradient Recalled (Fast SPGR) pulse sequences under free breathing (120 frames of 3.03 s each for a total acquisition time of 6 min, TR/TE = 3.46/1.10 ms; FOV: 400/320/120 mm, NEX = 0.69, voxel size 1.56 × 1.25 × 2.5 mm).

- A post-contrast 3D T₁-Fast SPGR sequence in breath-hold position (TR/TE = 4.48/2.41 ms, FOV: 440/352/179.2 mm, NEX = 0.7, voxel size 1.72 × 1.72 × 0.8 mm).

Image processing

Because no software or dedicated professional workstation currently allows the multimodal voxel-wise computation of PET and DCE parametric maps in PET-MRI, all data processing was performed on a stand-alone personal computer using in-house developed software written in Python (version 3.6; Python Software Foundation, www.python.org; libraries numpy, pandas, nibabel, Nilearn, Nipy, Scipy, Math). The general study workflow is provided in the Fig. 1. For each patient, the same image processing was performed as follows:

- Data normalization: [18F]FDG-PET and DCE-MRI data were first normalized to the 3D-T₁ reference isotropic space (i.e., the post-contrast 3D T₁-weighted MRI resampled to 2 mm³ isotropic). For this purpose, the dynamic PET data and the MR pre-contrast T₁-mapping data were resampled to the 3D-T₁ space (libraries Nilearn and nibabel), whereas the DCE data were motion-compensated (warping to the 3D-T₁ space) using the SyNQuick procedure (library Nipy, default parameters) implemented in Advanced Normalization Tools (ANTs) [38, 39].
- Tumor mask: the last frame of [18F]FDG-PET and DCE data, the pre-contrast T₁-mapping data, and the post-contrast 3D-T₁ data were masked semi-automatically with ITK-SNAP (<http://www.itksnap.org>), which implements an active contour-based



algorithm [40, 41], as follows: an intensity-grading feature image was first computed to define the lesion boundaries by thresholding the intensities of the input image into the background and foreground (region competition approach, in which the intensity values ranged from - 1 to 1 for background and foreground respectively); one or more spherical seeds were then placed on the feature image to initialize the segmentation task; and the iterative algorithm was launched to propagate the seeds, driven by regularity constraints and the image intensity properties. The resulting PET, DCE, T₁-mapping, and 3D-T₁ tumor masks were combined into a single multimodal tumor mask (library Nilearn) using a basic intersection operation.

- c) Arterial mask for image-based derived input function (IDIF): IDIF is non-invasive and has been validated against arterial sampling (the gold standard) in oncological patients [42]. IDIF was performed with the graphical user interface ITK-SNAP as follows: a small volume of interest (VOI) was carefully positioned on the center of the thoracic aorta to avoid spill-in and spill-over effects. The position was carefully chosen to fit within the FOVs of all the PET, T₁-mapping, and DCE fused data.
- d) Signal processing: the 4D-PET data were smoothed with an 8-mm Gaussian filter (library Nilearn), and

the DCE imaging data were converted to gadolinium plasma concentration $C(t)$ (libraries Nilearn, numpy, pandas) using the following equation [43]:

$$C(t) = \frac{1}{(1 - Hct)} \times \frac{-1}{r_{Gd} \times TR} \times \left[\frac{TR}{T_{10}} + Ln \left(\frac{\left(\frac{S(t)}{S_0} \times \frac{1 - E}{1 - \cos(\alpha)E} - 1 \right)}{\left(\frac{S(t)}{S_0} \times \cos(\alpha) \times \frac{1 - E}{1 - \cos(\alpha)E} - 1 \right)} \right) \right],$$

where S_0 and $S(t)$ are the signals measured before contrast-enhancement and at time t after contrast injection, Hct is the hematocrit level fixed at 0.45 [44], $r_{Gd} = 3.4 \text{ s}^{-1} \cdot \text{mM}^{-1}$ is the relaxivity of Dotarem at 3 T [45], $E = e^{-TR/T_{10}}$ where T_{10} is the estimated pre-contrast T_1 value in the voxel of interest, and α is the flip angle of the 3D Fast SPGR pulse sequence, set to 15° in our imaging protocol.

- e) Voxel-wise parametric maps computation: tumor and IDIF data were extracted from the masked 4D PET and DCE data, and the [18F]FDG PET ($K_1, k_2, k_3, v_b, MRGlu$) and DCE-MRI ($K_{trans}, v_e, K_{ep}, v_p$) kinetic parameters were finally computed by fitting the extracted data to the reference Sokoloff's ([18F]FDG PET) [7] and extended Tofts (DCE) [46]

compartmental models on a voxel-wise basis, using “in-house” second order Runge-Kutta procedures combined with Levenberg-Marquardt non-linear least-square fitting optimization (libraries numpy, pandas, scipy, math).

Statistical analysis

All the statistical analyses were performed with Python (version 3.6; Python Software Foundation, www.python.org) and R studio (version 3.4.0; R Project for Statistical Computing, <https://rstudio.com>).

Curve fitting errors of our in-house PET and DCE kinetic modeling implementation were assessed voxel-wise by computing the relative root mean square errors (Python, libraries numpy, and pandas), defined by $rRMSE = \frac{\|signal - \widehat{signal}\|_2}{\|signal\|_2}$ where *signal* is the measured signal and \widehat{signal} is the estimated signal after the fitting procedure. The PET and DCE kinetic microparameter values are expressed as median± IQR. After data transformation into z-score (zero mean and unit variance) and cleaning-up from outliers (z-score > 3), the PET-PET, DCE-DCE, and PET-DCE voxel-wise correlations were assessed for each tumor by estimating the related Spearman coefficients (*r_s*), along with their respective bootstrapped 95% confidence intervals (R studio, RVAideMemoire package, *n* = 1000 iterations). The absolute *r_s* estimated values (*|r_s|*) were considered low under 0.4, moderate between 0.4 and 0.7, and high above 0.7 [47].

Results

The general characteristics of the 14 patients are summarized in Table 1. Briefly, 9 were male, and 5 were female (sex ratio M/F = 1.8), aged 65.5 ± 10.6 years. The tumor localization was the right upper lobe for the majority of the patients (7 patients) or the left upper lobe (5 patients); the two remaining patients had the tumor in the right lower lobe and the right medium lobe, respectively. The estimated [18F]FDG PET and DCE kinetic parameters are summarized in Table 2. The voxel-wise curve-fitting metrics (fit errors) of the PET and DCE kinetic measurements are provided in Tables 3 and 4 and Fig. 2. For the 14 tumors (21,555 estimated voxels), the overall PET rRMSE was 10.3% (8.1; 14.3), corresponding to 89.3% of voxels with error under 20%. The overall DCE rRMSE was 31.8% (22.4; 46.6), corresponding to 73.3% of voxels with error under 45%. An illustration of the PET and DCE kinetic estimated parameter maps of the patient n°9, together with their related curve-fitting statistics, is provided in Fig. 3. The correlation analyses showed wide variability in the PET-PET, DCE-DCE, and PET-DCE correlations (Figs. 4 and 5 and supplementary material). The PET-PET and DCE-DCE correlations were mainly moderate to strong for all the tumors but with high individual variabilities (Fig. 4 and supplementary material). When considering the PET-DCE correlations exclusively, the 14 tumors showed weak (*|r_s|* < 0.4) to moderate (0.4 ≤ *|r_s|* < 0.7) correlations exclusively (Fig. 5 and supplementary material).

Table 2 Estimated PET and DCE kinetic parameters. Kinetic parameters are expressed as median (IQR)

Tumors	PET parameters					DCE parameters			
	K ₁ (ml g ⁻¹ min ⁻¹)	k ₂ (min ⁻¹)	k ₃ (min ⁻¹)	MRGlu (μmol g ⁻¹ min ⁻¹)	v _b	K _{trans} (min ⁻¹)	v _e	K _{ep} (min ⁻¹)	v _p
1	0.22 (0.18-0.26)	0.71 (0.54-0.81)	0.13 (0.1-0.14)	0.15 (0.12-0.17)	0.05 (0.03-0.07)	0.30 (0.14-0.60)	0.68 (0.42-1.0)	0.60 (0.28-1.19)	0.008 (0.0-0.05)
2	0.26 (0.22-0.32)	0.68 (0.45-1.03)	0.15 (0.10-0.20)	0.24 (0.19-0.26)	0.05 (0.03-0.06)	0.84 (0.67-1.17)	1.0 (1.0-1.0)	0.85 (0.68-1.18)	0.40 (0.19-0.68)
3	0.08 (0.06-0.11)	0.31 (0.22-0.44)	0.09 (0.05-0.14)	0.09 (0.07-0.10)	0.13 (0.09-0.18)	0.17 (0.07-0.60)	0.33 (0.09-1.0)	0.56 (0.27-27.7)	0.03 (0.0-0.12)
4	0.15 (0.12-0.18)	1.09 (0.85-1.40)	0.033 (0.029-0.036)	0.026 (0.022-0.032)	0.084 (0.076-0.093)	0.74 (0.25-1.36)	0.63 (0.33-1.0)	1.21 (0.57-2.66)	0.15 (0.04-0.36)
5	0.19 (0.15-0.24)	0.57 (0.46-0.77)	0.19 (0.15-0.24)	0.35 (0.30-0.38)	0.09 (0.08-0.10)	0.07 (0.05-0.13)	0.17 (0.13-0.21)	0.47 (0.30-0.74)	0.02 (0.009-0.024)
6	0.38 (0.34-0.42)	1.30 (1.14-1.47)	0.089 (0.068-0.109)	0.11 (0.09-0.14)	0.066 (0.057-0.077)	0.84 (0.36-1.75)	1.0 (0.47-1.0)	1.30 (0.66-2.25)	0.05 (0.0-1.0)
7	0.14 (0.12-0.16)	0.41 (0.35-0.5)	0.028 (0.022-0.034)	0.053 (0.048-0.06)	0.109 (0.084-0.13)	0.06 (0.04-0.14)	0.95 (0.32-1.0)	0.12 (0.06-0.23)	0.12 (0.06-0.23)
8	0.11 (0.07-0.13)	0.66 (0.44-0.72)	0.08 (0.05-0.1)	0.063 (0.045-0.084)	0.18 (0.16-0.19)	0.52 (0.15-1.06)	0.19 (0.03-0.62)	1.90 (1.20-3.78)	0.0 (0.0-0.08)
9	0.22 (0.17-0.26)	0.55 (0.47-0.61)	0.071 (0.059-0.088)	0.14 (0.11-0.19)	0.05 (0.03-0.07)	0.32 (0.17-0.53)	0.52 (0.29-0.77)	0.63 (0.45-0.92)	0.034 (0.0-0.09)
10	0.26 (0.20-0.32)	0.63 (0.45-0.83)	0.08 (0.05-0.14)	0.22 (0.14-0.34)	0.11 (0.09-0.14)	1.06 (0.64-1.47)	1.0 (0.38-1.0)	1.25 (0.91-2.67)	0.25 (0.0003-0.81)
11	0.15 (0.13-0.18)	0.48 (0.34-0.65)	0.11 (0.09-0.14)	0.16 (0.13-0.19)	0.09 (0.06-0.13)	0.81 (0.34-1.28)	0.74 (0.33-1.0)	1.23 (0.90-1.65)	0.08 (0.0001-0.27)
12	0.29 (0.22-0.36)	1.29 (0.80-1.96)	0.32 (0.19-0.57)	0.33 (0.22-0.43)	0.05 (0.03-0.08)	0.32 (0.12-0.77)	0.29 (0.15-0.65)	1.00 (0.54-1.69)	0.04 (0.001-0.11)
13	0.33 (0.23-0.44)	0.77 (0.55-1.04)	0.1 (0.06-0.14)	0.21 (0.15-0.25)	0.097 (0.077-0.14)	1.02 (0.62-1.43)	1.0 (0.85-1.0)	1.17 (0.78-1.57)	0.05 (0.0-0.22)
14	0.31 (0.27-0.35)	0.68 (0.57-0.77)	0.07 (0.05-0.08)	0.14 (0.11-0.17)	0.052 (0.032-0.072)	0.27 (0.14-0.57)	0.53 (0.36-1.0)	0.60 (0.35-0.80)	0.008 (0.0-0.03)

Table 3 Curve fitting metrics for PET kinetic modeling

PET	Relative RMSE	Fraction of voxels in percent		
		Relative RMSE ≤ 20%	20% < relative RMSE ≤ 45%	45% < Relative RMSE
1	13.4 (10; 20.3)	74%	23%	3%
2	9.0 (6.9; 12.2)	99.6%	0.4%	0%
3	18.1 (12.9; 26.8)	57%	36%	7%
4	34.3 (29; 39)	0%	94.8%	5.2%
5	16.1 (14; 18.1)	87.2%	12.8%	0%
6	23.7 (19.6; 27.3)	27%	72%	1%
7	49.2 (44.1; 54)	0%	29%	71%
8	43.5 (39.7; 51.2)	0%	57.6%	42.4%
9	8.5 (7.4; 9.8)	98.2%	1.8%	0%
10	12.3 (9.8; 15.3)	95.3%	4.7%	0%
11	15.5 (11.5; 19.5)	77.8%	22.2%	0%
12	9.5 (7.6; 11.8)	99.7%	0.3%	0%
13	9.2 (7.7; 11.3)	99.4%	0.6%	0%
14	8.2 (7.4; 9.2)	100%	0%	0%
All	10.3 (8.1; 14.3)	89.3%	7.6%	3.1%

Relative RMSE data are expressed as median (IQR)

MRGlu was positively correlated to k_3 in all tumors and inversely correlated with K_{trans} , v_p , or v_b in the majority of tumors. The 3D parametric maps clearly showed regional decoupling patterns of hypoperfused (K_{trans} or K_1) and poor vascularized areas (v_b or v_p) with high metabolic enzymatic activity (k_3) in five tumors, as illustrated in Fig. 6 (tumors 1, 5, 12, 13, and 14).

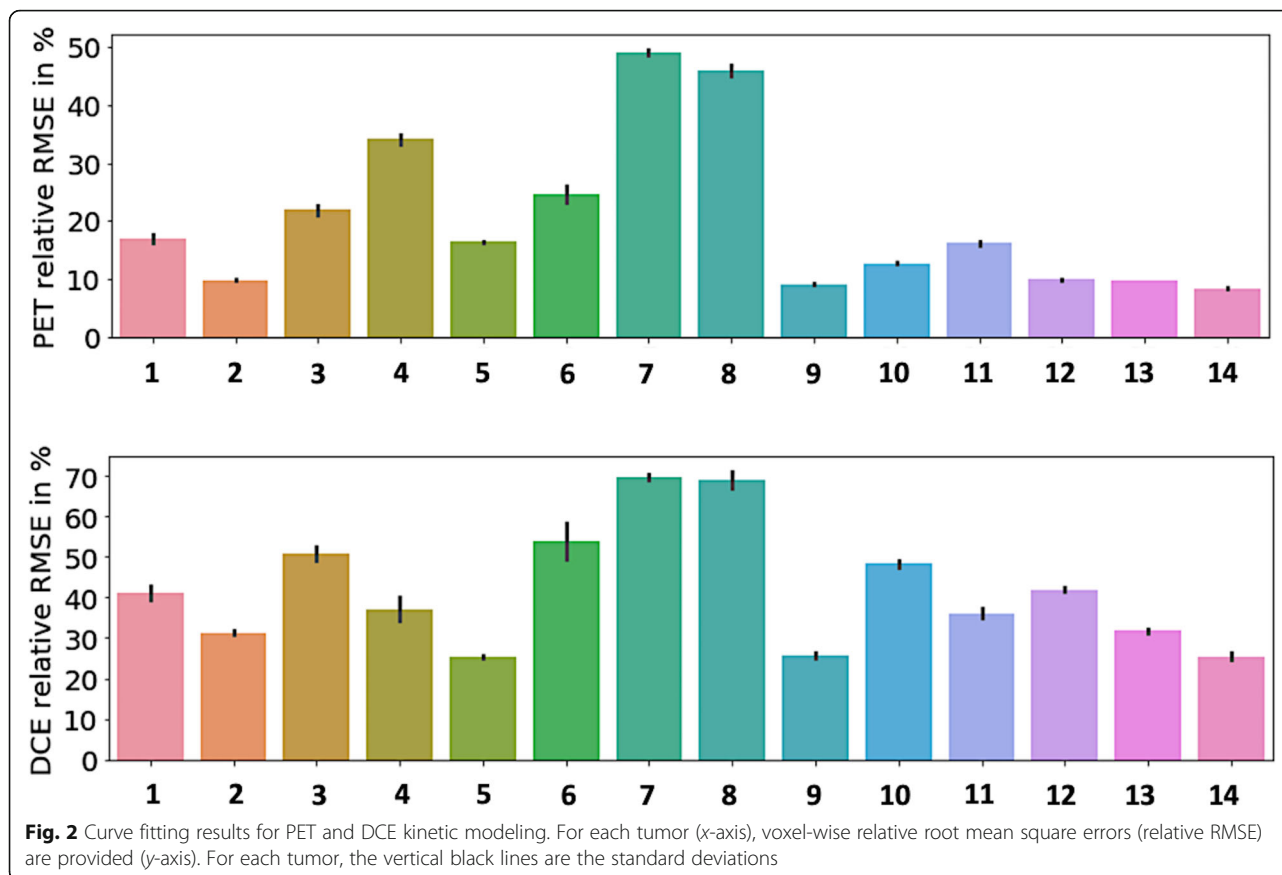
Discussion

This simultaneous dynamic PET-DCE MRI study shows that dynamic PET and DCE monotonic correlations, measured in exactly the same conditions, are highly variable at the tumor level in treatment-naïve NSCLC. [18F]FDG dynamic PET-DCE MRI has the unique capability to capture the individual tumor biological behavior of NSCLC. Vascularity and perfusion properties are

Table 4 Curve fitting metrics for DCE kinetic modeling

DCE	Relative RMSE	Number of voxels in percent		
		Relative RMSE ≤ 20%	20% < relative RMSE ≤ 45%	45% < relative RMSE
1	35 (26; 51.5)	6.6%	60%	33.4%
2	30.2 (25; 36)	8.3%	87.1%	4.6%
3	46.6 (32.4; 65.3)	3.7%	44%	52.3%
4	29.3 (22.1; 46.9)	21.3%	50%	28.7%
5	23.8 (20.5; 28.5)	21.6%	76%	2.4%
6	49.1 (39.5; 68.5)	1.2%	43%	55.8%
7	68.3 (63.4; 73.2)	0%	0%	100%
8	65.8 (54.9; 84.9)	0%	8.8%	91.2%
9	19.5 (14.2; 29.6)	51.5%	37%	11.5%
10	42.5 (35; 56)	0.1%	56%	43.9%
11	29.8 (23.1; 41.7)	14.5%	64.9%	20.6%
12	36.7 (28; 51.4)	5%	61.4%	33.6%
13	27 (19.7; 40.8)	26.7%	54.2%	19.1%
14	21.1 (15; 29.6)	46.3%	42.5%	11.2%
All	31.8 (22.4; 46.6)	18.6%	54.7%	26.7%

Relative RMSE data are expressed as median (IQR)



spatially variable in NSCLC [48, 49]. This wide variability has been recently highlighted in [18F]FDG PET compartmental analyses [50] and was qualitatively illustrated in our combined dynamic PET-DCE MRI study.

As expected, MRglu and k_3 PET microparameters were positively correlated in all the tumors, emphasizing the expected close relationship between the regional metabolic and phosphorylated rates of glucose. In more than half the tumors, both MRglu and k_3 were inversely correlated to K_{trans} , v_p , and v_b , suggesting high metabolic but low perfused/vascularized cells, a well-known hallmark of tumor hypoxia or aggressiveness [20]. Recent head and neck ^{18}F -FMISO [51] and preclinical VX-2 ^{13}N - NH_3 [52] PET/DCE MRI studies showed weak correlation between K_1 and K_{trans} perfusion parameters. In our NSCLC [18F]FDG PET/DCE-MRI clinical study, the K_1 - K_{trans} correlations were also mainly weak. This general trend is not surprising considering the three following key concepts: First, perfusion reflects a weighted mixture of blood flow and permeability-surface area product [13, 53, 54] that depends, in the case of fixed flow and microvascular characteristics, on the tracer's exchange properties—[18F]FDG is actively transported across the cellular membrane, whereas Gd is a purely extra cellular diffusive contrast agent. Second, the DCE

Tofts models [46, 55] do not consider the intra-cellular space (ICS), whereas standard compartmental PET models [7] do not distinguish the extravascular extracellular space (EES) from the ICS, assuming steady state between EES and ICS at time of injection. Consequently, K_1 depends on a mixed perfusion-extraction weighting of [18F]FDG that may, in the case of high metabolic rate conditions, overestimate the perfusion component [53].

Our study has several limitations. Our data sample was limited to 14 biopsy-proven NSCLC. Also, because pre-contrast T_1 -mapping was limited to 6 slices per tumor for practical considerations, we could not capture the multimodal correlations of the entire tumor volume. Compared to PET, DCE kinetic modeling showed higher voxel-wise fit errors. It is well-known that many factors hamper the accuracy of DCE pharmacokinetic modeling, making this approach highly challenging in clinical practice [56–58]. For illustration, analyzing the same patient and imaging data with multiple different commercially available software packages was reported to lead to within-patient variabilities of up to 74% in DCE-MRI measurements [59]. In our study, motion corruption was probably the major explanation of the measurement errors. The high temporal resolution of the DCE frames emphasized the motion corruption effects, which were

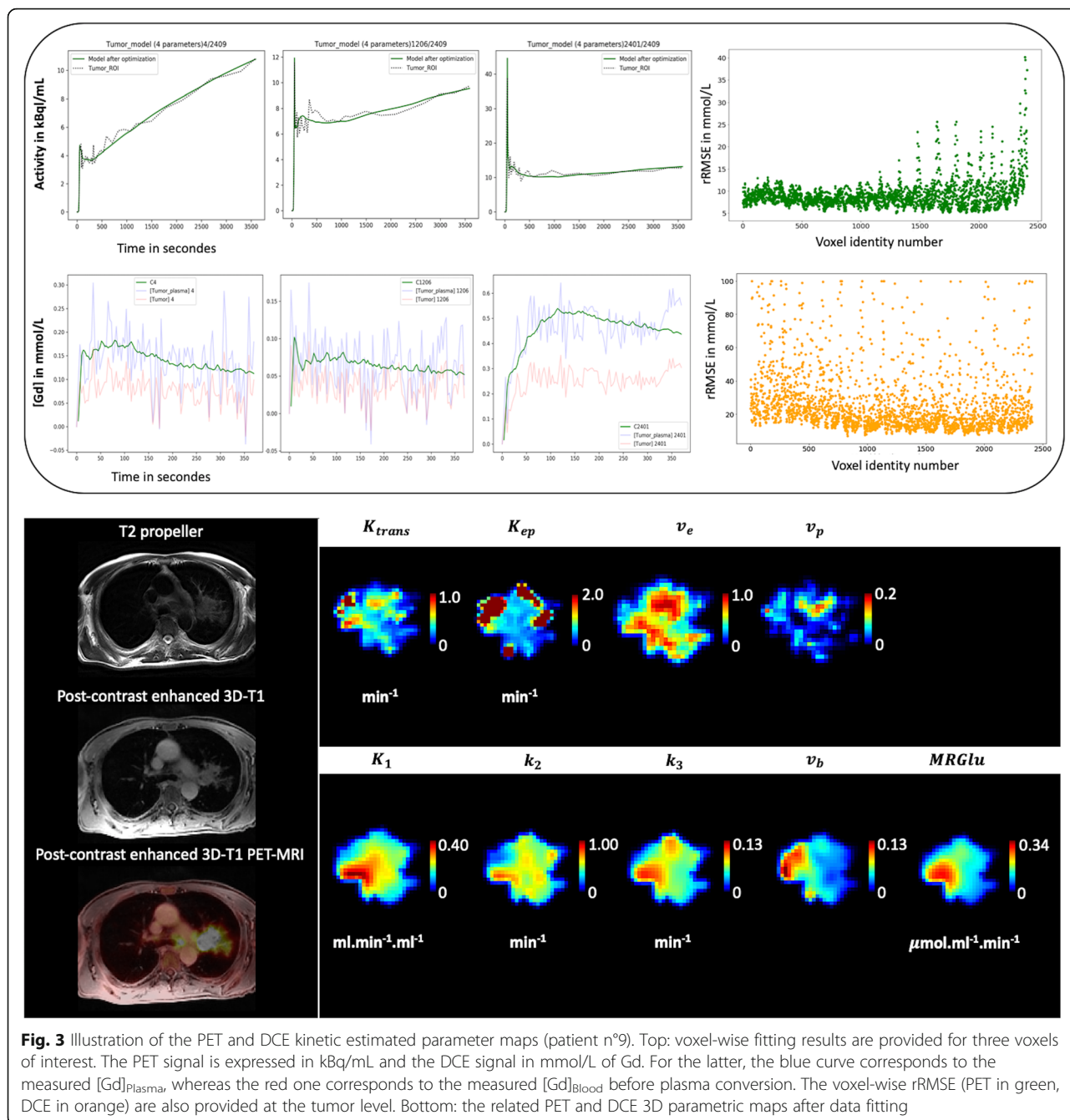


Fig. 3 Illustration of the PET and DCE kinetic estimated parameter maps (patient n°9). Top: voxel-wise fitting results are provided for three voxels of interest. The PET signal is expressed in kBq/mL and the DCE signal in mmol/L of Gd. For the latter, the blue curve corresponds to the measured [Gd]_{plasma}, whereas the red one corresponds to the measured [Gd]_{blood} before plasma conversion. The voxel-wise rRMSE (PET in green, DCE in orange) are also provided at the tumor level. Bottom: the related PET and DCE 3D parametric maps after data fitting

only partially compensated by our standard motion correction method. For our study, the mean fraction of outliers used for the correlation analyses was under 10% among all the 14 tumors ($7.8\% \pm 2.8\%$). A better availability of advanced motion compensation techniques [60] would be of particular interest. We did not include the K_i PET parameter but instead used the MRGlu parameter, which is the K_i -glycaemia product normalized by the lumped constant (LC). We justified this choice because LC is arbitrarily set to 1 in oncology studies (the unknown true LC precludes any other value) [61, 62]

making MRGlu a basic multiple of K_i . A dual arterial input implementation has been recently proposed in few CT or MR-based perfusion studies [63–67], based on the fact that lung tumors may have a dual blood supply [68]. The selection of the correct model for the right tumor is limited by what is named the “mixed tissue conundrum” [69] and remains mainly driven by both its bias-variance tradeoff and clinical relevance. In this way, DCE Tofts models have become standards in oncology [70, 71] and have shown preclinical and clinical relevance in lung cancer specifically [15, 16, 72]. The dual

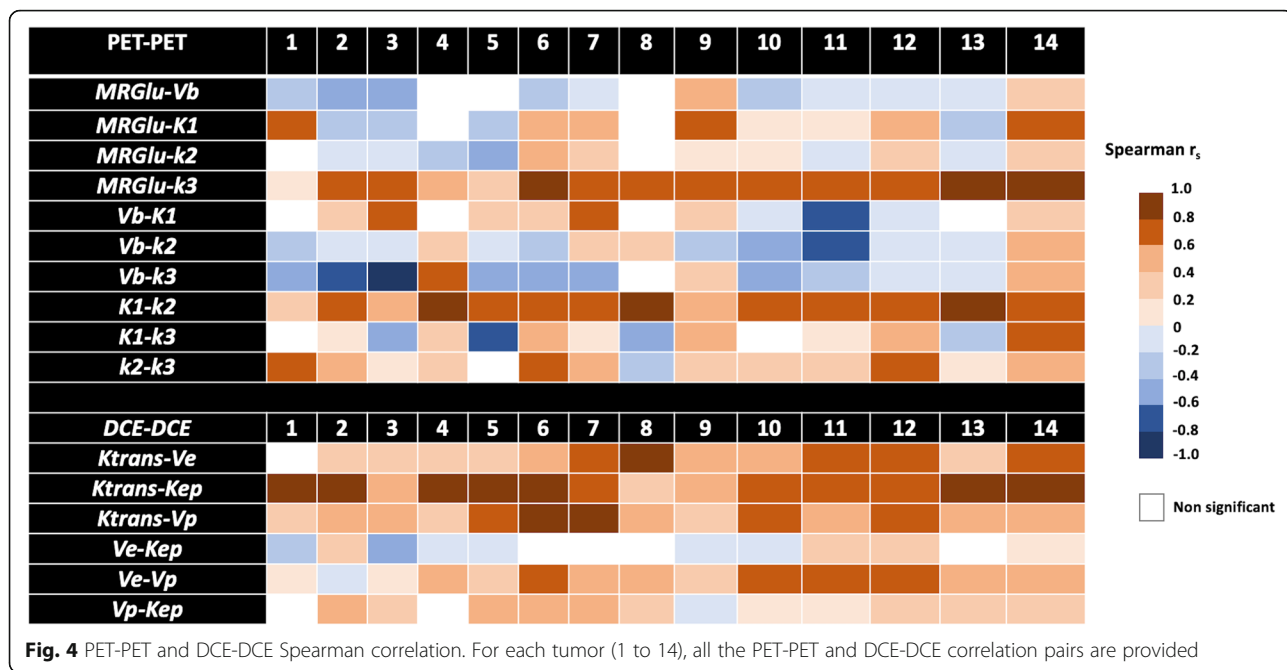


Fig. 4 PET-PET and DCE-DCE Spearman correlation. For each tumor (1 to 14), all the PET-PET and DCE-DCE correlation pairs are provided

AIF, however, has never been validated for dynamic PET analyses and therefore cannot be considered as a reference. Even though the majority of the included tumors were in the upper lobes, our results are prone to potential uncertainties related to respiratory motion artifacts and the uncertain efficacy of our motion compensation

procedure. Finally, voxel-wise comparisons were performed on data resampled at 2 mm³ resolution and an 8-mm 3D Gaussian smoothing applied to the PET modality. The 8 mm Gaussian post-filtering was applied to the PET data to denoise the PET images and regularize the motion-corrupted time-varying activity curves. To

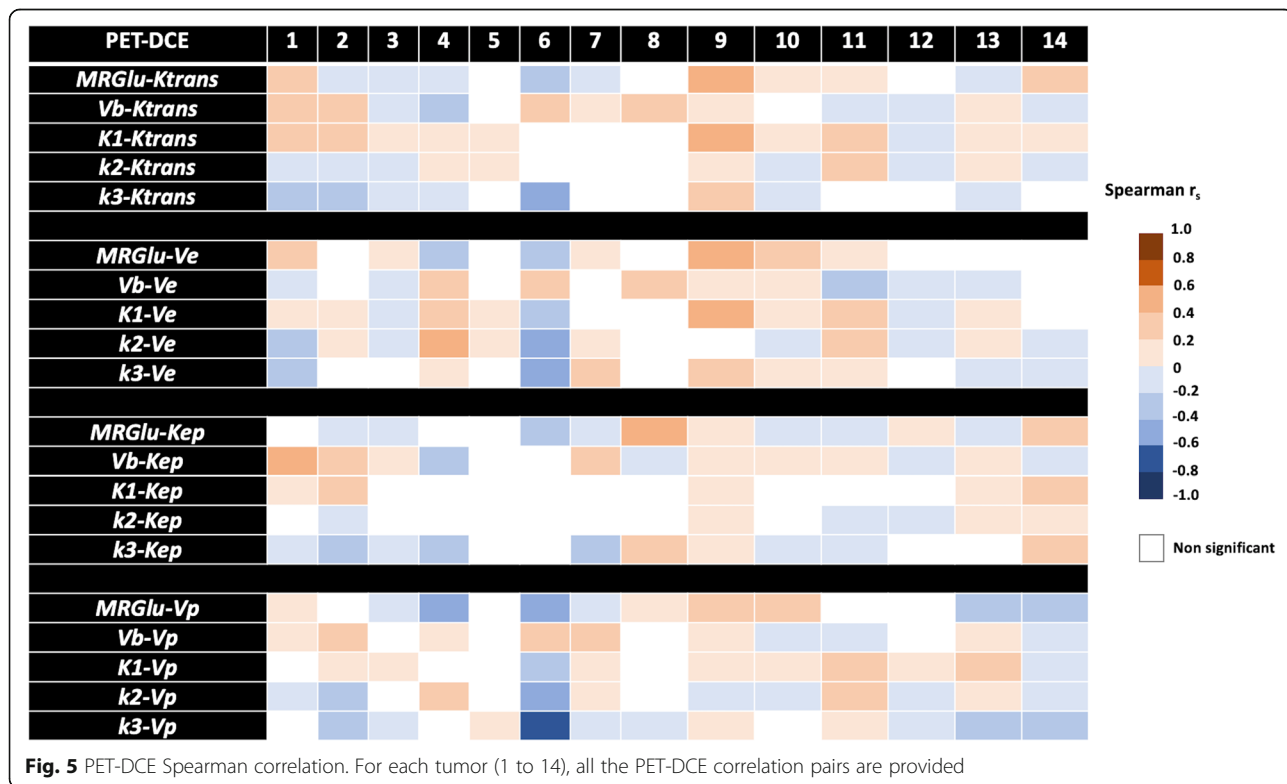
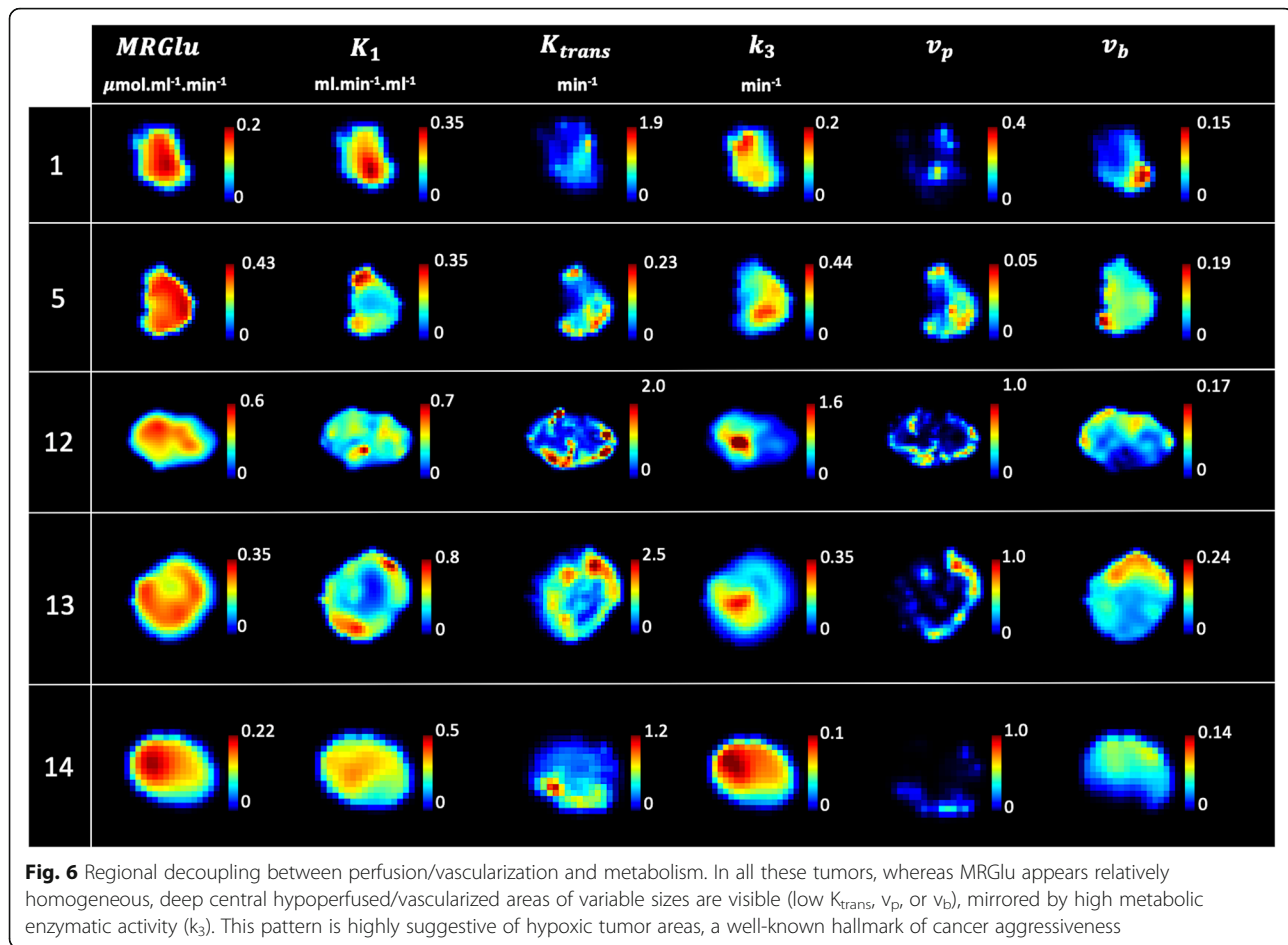


Fig. 5 PET-DCE Spearman correlation. For each tumor (1 to 14), all the PET-DCE correlation pairs are provided



some extent, neighboring voxels are expected to share similar behavior in a lesion of interest, and the smoothing process emphasizes this structural consistency at the regional intra-tumor level by reducing the granularity of noise in the data. Moreover, Gaussian kernels make the distribution of the data more reliable for further statistical analyses: for example, state-of-the-art multimodal neuroimaging analyses using statistical parametrical maps (SPM) typically use smoothing of the PET data before voxel-wise analyses, and wider smoothing kernels are frequently used. These pre-processing steps are not a problem for multimodal analyses of thin cortical structures at the voxel level (for example, see [73]). Despite the use of Gaussian smoothing on PET data, the 3D maps of both the PET and DCE kinetic parameters showed structured and consistent intra-tumor regional subparts, as illustrated in Fig. 6.

Despite these limitations, this study shows that simultaneous dynamic PET-MRI is feasible in NSCLC patients. This tends to demonstrate the potential application of simultaneous PET/MRI imaging to further characterize the individual biological tumor behavior in NSCLC in clinical practice. However, further studies are necessary to demonstrate the clinical utility of this approach.

Conclusion

A dynamic “one-stop shop” procedure applied to NSCLC is technically feasible in clinical practice. Simultaneously acquired PET and DCE kinetic parameters assessed in a combined manner are not highly correlated in NSCLC, and these correlations showed a wide variability between tumors and patients. These results tend to suggest that PET and DCE kinetic parameters might provide complementary information for tumor characterization, and this might make PET-MRI a unique tool to characterize the individual tumor biological behavior in NSCLC.

Supplementary information

Supplementary information accompanies this paper at <https://doi.org/10.1186/s13550-020-00671-9>.

Additional file 1. Voxel-wise Spearman correlation coefficients (r_s) together with their respective bootstrap intervals ($n = 1000$ replications). Values in red correspond to statistically non-significant results.

Acknowledgements

We would like to particularly thank Henri Souchay and Isabelle Dufour from GE Healthcare; Pernelle Lavaud, Frank Aboubakar, Charles Naltet, Muriel Malgogne, Céline Casale, and Thibault Raoult from Gustave Roussy; Pauline Pradere from Hopital Marie Lannelongue; and Philippe Gervais, Ghislaine

Latapie, Martine Gouel, Christine Manciot, Christine Baron, Bérangère Eyl, Véronique Maison, Stéphanie Beau, Marion Petit, Charlotte Ferrand, Thierry Lekieffre, Yoann Fontyn, Kevin Phansavath, and Vincent Brulon from the Service Hospitalier Frédéric Joliot-CEA for their help in completing this study. The authors also thank Mark Symms for his useful comments and English corrections.

Authors' contributions

All authors: Design, acquisition analysis. Revising for intellectual content. Final approval. Agreement to be accountable for all aspects of this work (accuracy and integrity of any part of the work). In addition: Kinetic parameter programming: Florent L. Besson and Sylvain Faure. MRI sequence optimization: Florent L. Besson and Brice Fernandez. Patient recruitment and/or surgical procedure: Olaf Mercier, Andrei Seferian, Xavier Mignard, Sacha Musnot, Cécile le Péchoux, Caroline Caramella, Angela Botticella, Antonin Levy, Florence Parent: Sophie Bullifon, David Montani, Delphine Mitilian, Elie Fadel, David Planchard, and Benjamin Besse. Histological confirmation: Maria-Rosa Ghigna-Bellinzoni

Funding

The imaging facility (SHFJ) where acquisitions were performed has received funding from the French programs "Investissements d'avenir" run by the "Agence Nationale de la Recherche" and "Infrastructure d'avenir en Biologie Santé" France Life Imaging (grant ANR-11-INBS-0006).

Availability of data and materials

The datasets generated and analyzed during the current study are not publicly available, in accordance with the General Data Protection Regulation (GDPR) of the European Union, but are available from the corresponding author on request, after justification that meets the GDPR principles.

Ethics approval and consent to participate

All procedures performed were in accordance with the ethical standards of the institutional research committee and with the principles of the 1964 Declaration of Helsinki and its later amendments. The local institutional review board (SHFJ Research Steering Committee, DRF/JOLIOT/SHFJ/2020/10) approved this study, and all patients signed a written informed consent.

Consent for publication

Not applicable

Competing interests

Brice Fernandez (second author) is a PET/MR lead scientist employed by GE Healthcare.

Author details

¹Université Paris-Saclay, CEA, CNRS, Inserm, BioMAPs, 91401 Orsay, France. ²Department of Biophysics and Nuclear Medicine-Molecular Imaging, Hôpitaux Universitaires Paris-Saclay, Assistance Publique-Hôpitaux de Paris, CHU Bicêtre, 94270 Le Kremlin-Bicêtre, France. ³School of Medicine, Université Paris-Saclay, Le Kremlin-Bicêtre, France. ⁴Applications and Workflow, GE Healthcare, Orsay, France. ⁵Laboratoire de Mathématiques d'Orsay, CNRS, Université Paris-Saclay, 91405 Orsay, France. ⁶Department of Thoracic and Vascular Surgery and Heart-Lung Transplantation, Marie Lannelongue Hospital, 92350 Le Plessis Robinson, France. ⁷Service de Pneumologie, Centre de Référence de l'Hypertension Pulmonaire, Hôpitaux Universitaires Paris-Saclay, Assistance Publique-Hôpitaux de Paris, 94270 Le Kremlin-Bicêtre, France. ⁸Inserm UMR_S999, Marie Lannelongue Hospital, 92350 Le Plessis Robinson, France. ⁹Department of Radiation Oncology, Institut d'Oncologie Thoracique (IOT), Gustave Roussy, Université Paris Saclay, Villejuif, France. ¹⁰Department of Radiology, Institut d'Oncologie Thoracique (IOT), Gustave Roussy, Université Paris Saclay, Villejuif, France. ¹¹Department of Oncology, Institut d'Oncologie Thoracique (IOT), Gustave Roussy, Université Paris Saclay, Villejuif, France. ¹²Department of Pathology, Marie Lannelongue Hospital, 92350 Le Plessis Robinson, France.

Received: 23 March 2020 Accepted: 14 July 2020

Published online: 30 July 2020

References

- Zaidi H, Ojha N, Morich M, Griesmer J, Hu Z, Maniawski P, et al. Design and performance evaluation of a whole-body Ingenuity TF PET-MRI system. *Phys Med Biol*. 2011;56:3091–106.
- Delso G, Furst S, Jakoby B, Ladebeck R, Ganter C, Nekolla SG, et al. Performance measurements of the Siemens mMR integrated whole-body PET/MR scanner. *J Nucl Med*. 2011;52:1914–22.
- Czernin J, Ta L, Herrmann K. Does PET/MR imaging improve cancer assessments? Literature evidence from more than 900 patients. *J Nucl Med*. 2014;55:595–625.
- Padhani AR, Miles KA. Multiparametric imaging of tumor response to therapy. *Radiology*. 2010;256:348–64.
- Tunariu N, Kaye SB, de Souza NM. Functional imaging: what evidence is there for its utility in clinical trials of targeted therapies? *Br J Cancer*. 2012;106:619–28.
- Lin G, Chung Y-L. Current opportunities and challenges of magnetic resonance spectroscopy, positron emission tomography, and mass spectrometry imaging for mapping cancer metabolism *in vivo*. *Biomed Res Int*. 2014;2014:1–13.
- Sokoloff L, Reivich M, Kennedy C, Des Rosiers MH, Patlak CS, Pettigrew KD, et al. The [¹⁴C]deoxyglucose method for the measurement of local cerebral glucose utilization: theory, procedure, and normal values in the conscious and anesthetized albino rat. *J Neurochem*. 1977;28:897–916.
- Dimitrakopoulou-Strauss A, Strauss LG, Burger C, Rühl A, Irngartinger G, Stremmel W, et al. Prognostic aspects of 18F-FDG PET kinetics in patients with metastatic colorectal carcinoma receiving FOLFOX chemotherapy. *J Nucl Med*. 2004;45:1480–7.
- Strauss LG, Klippel S, Pan L, Schönleben K, Haberkorn U, Dimitrakopoulou-Strauss A. Assessment of quantitative FDG PET data in primary colorectal tumours: which parameters are important with respect to tumour detection? *Eur J Nucl Med Mol Imaging*. 2007;34:868–77.
- Dimitrakopoulou-Strauss A, Strauss LG, Egerer G, Vasamilliette J, Schmitt T, Haberkorn U, et al. Prediction of chemotherapy outcome in patients with metastatic soft tissue sarcomas based on dynamic FDG PET (dPET) and a multiparameter analysis. *Eur J Nucl Med Mol Imaging*. 2010;37:1481–9.
- Epelbaum R, Frenkel A, Haddad R, Sikorski N, Strauss LG, Israel O, et al. Tumor aggressiveness and patient outcome in cancer of the pancreas assessed by dynamic 18F-FDG PET/CT. *J Nucl Med*. 2013;54:12–8.
- Yang Z, Zan Y, Zheng X, Hai W, Chen K, Huang Q, et al. Dynamic FDG-PET imaging to differentiate malignancies from inflammation in subcutaneous and *in situ* mouse model for non-small cell lung carcinoma (NSCLC). Tagliabue E, editor. *PLoS One*. 2015;10:e0139089.
- Cuenod CA, Balvay D. Perfusion and vascular permeability: basic concepts and measurement in DCE-CT and DCE-MRI. *Diagnostic and Interventional Imaging*. 2013;94:1187–204.
- Kim J-H, Kim CK, Park BK, Park SY, Huh SJ, Kim B. Dynamic contrast-enhanced 3-T MR imaging in cervical cancer before and after concurrent chemoradiotherapy. *Eur Radiol*. 2012;22:2533–9.
- Cheng JC-H, Yuan A, Chen J-H, Lu Y-C, Cho K-H, Wu J-K, et al. Early detection of Lewis lung carcinoma tumor control by irradiation using diffusion-weighted and dynamic contrast-enhanced MRI. Lin C-P, editor. *PLoS One*. 2013;8:e62762.
- Tao X, Wang L, Hui Z, Liu L, Ye F, Song Y, et al. DCE-MRI Perfusion and permeability parameters as predictors of tumor response to CCRT in patients with locally advanced NSCLC. *Sci Rep*. 2016;6:35569.
- Hatzoglou V, Tisnado J, Mehta A, Peck KK, Daras M, Omuro AM, et al. Dynamic contrast-enhanced MRI perfusion for differentiating between melanoma and lung cancer brain metastases. *Cancer Med*. 2017;6:761–7.
- Huang Y-S, Chen JL-Y, Hsu F-M, Huang J-Y, Ko W-C, Chen Y-C, et al. Response assessment of stereotactic body radiation therapy using dynamic contrast-enhanced integrated MR-PET in non-small cell lung cancer patients. *J Magn Reson Imaging*. 2018;47:191–9.
- Fouad YA, Aanei C. Revisiting the hallmarks of cancer. *Am J Cancer Res*. 2017;7:1016–36.
- Miles KA. Warburg revisited: imaging tumour blood flow and metabolism. *Cancer Imaging*. 2008;8:81–6.

21. Heusch P, Buchbender C, Kohler J, Nensa F, Gauler T, Gomez B, et al. Thoracic staging in lung cancer: prospective comparison of 18F-FDG PET/MR imaging and 18F-FDG PET/CT. *J Nucl Med*. 2014;55:373–8.
22. Schaarschmidt B, Buchbender C, Gomez B, Rubbert C, Hild F, Köhler J, et al. Thoracic staging of non-small-cell lung cancer using integrated 18F-FDG PET/MR imaging: diagnostic value of different MR sequences. *Eur J Nucl Med Mol Imaging*. 2015;42:1257–67.
23. Ohno Y, Koyama H, Yoshikawa T, Takenaka D, Seki S, Yui M, et al. Three-way comparison of whole-body MR, coregistered whole-body FDG PET/MR, and integrated whole-body FDG PET/CT imaging: TNM and stage assessment capability for non-small cell lung cancer patients. *Radiology*. 2015;275:849–61.
24. Schaarschmidt BM, Grueneisen J, Metzenmacher M, Gomez B, Gauler T, Roesel C, et al. Thoracic staging with 18F-FDG PET/MR in non-small cell lung cancer – does it change therapeutic decisions in comparison to 18F-FDG PET/CT? *Eur Radiol*. 2017;27:681–8.
25. Kirchner J, Sawicki LM, Nensa F, Schaarschmidt BM, Reis H, Ingenwerth M, et al. Prospective comparison of 18F-FDG PET/MRI and 18F-FDG PET/CT for thoracic staging of non-small cell lung cancer. *Eur J Nucl Med Mol Imaging*. 2019;46:437–45.
26. Regier M, Derlin T, Schwarz D, Laqmani A, Henes FO, Groth M, et al. Diffusion weighted MRI and 18F-FDG PET/CT in non-small cell lung cancer (NSCLC): does the apparent diffusion coefficient (ADC) correlate with tracer uptake (SUV)? *Eur J Radiol*. 2012;81:2913–8.
27. Heusch P, Köhler J, Wittsack H-J, Heusinger TA, Buchbender C, Poeppel TD, et al. Hybrid [18F]-FDG PET/MRI including non-Gaussian diffusion-weighted imaging (DWI): preliminary results in non-small cell lung cancer (NSCLC). *Eur J Radiol*. 2013;82:2055–60.
28. Schaarschmidt BM, Buchbender C, Nensa F, Grueneisen J, Gomez B, Köhler J, et al. Correlation of the apparent diffusion coefficient (ADC) with the standardized uptake value (SUV) in lymph node metastases of non-small cell lung cancer (NSCLC) patients using hybrid 18F-FDG PET/MRI. *Byrnes KR, editor. PLoS One*. 2015;10:e0116277.
29. Metz S, Ganter C, Lorenzen S, van Marwick S, Holzapfel K, Herrmann K, et al. Multiparametric MR and PET imaging of intratumoral biological heterogeneity in patients with metastatic lung cancer using voxel-by-voxel analysis. *Muñoz-Barrutia A, editor. PLoS One*. 2015;10:e0132386.
30. Iizuka Y, Matsuo Y, Umeoka S, Nakamoto Y, Ueki N, Mizowaki T, et al. Prediction of clinical outcome after stereotactic body radiotherapy for non-small cell lung cancer using diffusion-weighted MRI and 18F-FDG PET. *Eur J Radiol*. 2014;83:2087–92.
31. Hunter GJ, Hamberg LM, Choi N, Jain RK, McCloud T, Fischman AJ. Dynamic T1-weighted magnetic resonance imaging and positron emission tomography in patients with lung cancer: correlating vascular physiology with glucose metabolism. *Clin Cancer Res*. 1998;4:949–55.
32. Tateishi Y, Nishihara H, Tsukamoto E, Morikawa T, Tamaki N, Miyasaka K. Lung tumors evaluated with FDG-PET and dynamic CT: the relationship between vascular density and glucose metabolism. *J Comput Assist Tomogr*. 2002;26:185–90.
33. Hoekstra CJ, Stroobants SG, Hoekstra OS, Smit EF, Vansteenkiste JF, Lammertsma AA. Measurement of perfusion in stage IIIA-N2 non-small cell lung cancer using H₂(15)O and positron emission tomography. *Clin Cancer Res*. 2002;8:2109–15.
34. Miles KA, Griffiths MR, Keith CJ. Blood flow-metabolic relationships are dependent on tumour size in non-small cell lung cancer: a study using quantitative contrast-enhanced computer tomography and positron emission tomography. *Eur J Nucl Med Mol Imaging*. 2006;33:22–8.
35. Zhang J, Chen L, Chen Y, Wang W, Cheng L, Zhou X, et al. Tumor vascularity and glucose metabolism correlated in adenocarcinoma, but not in squamous cell carcinoma of the lung. *Zhang Z, editor. PLoS One*. 2014;9:e91649.
36. Boellaard R, Delgado-Bolton R, Oyen WJG, Giammarile F, Tatsch K, Eschner W, et al. FDG PET/CT: EANM procedure guidelines for tumour imaging: version 2.0. *Eur J Nucl Med Mol Imaging*. 2015;42:328–54.
37. Slavin GS, Stainsby JA. True T1 mapping with SMART1Map (saturation method using adaptive recovery times for cardiac T1 mapping): a comparison with MOLLI. *J Cardiovasc Magn Reson*. 2013;15:P3, 1532-429X-15-S1-P3.
38. Avants B, Epstein C, Grossman M, Gee J. Symmetric diffeomorphic image registration with cross-correlation: evaluating automated labeling of elderly and neurodegenerative brain. *Med Image Anal*. 2008;12:26–41.
39. Avants BB, Tustison NJ, Stauffer M, Song G, Wu B, Gee JC. The Insight Toolkit image registration framework. *Frontiers in Neuroinformatics* [Internet]. 2014 [cited 2019 May 28];8. Available from: <http://journal.frontiersin.org/article/10.3389/fninf.2014.00044/abstract>.
40. Yushkevich PA, Piven J, Hazlett HC, Smith RG, Ho S, Gee JC, et al. User-guided 3D active contour segmentation of anatomical structures: significantly improved efficiency and reliability. *Neuroimage*. 2006;31:1116–28.
41. Besson FL, Henry T, Meyer C, Chevance V, Roblot V, Blanchet E, et al. Rapid contour-based segmentation for ¹⁸F-FDG PET imaging of lung tumors by using ITK-SNAP: comparison to expert-based segmentation. *Radiology*. 2018;288:277–84.
42. de Geus-Oei L-F, Visser EP, Krabbe PFM, van Hoorn BA, Koenders EB, Willemsen AT, et al. Comparison of image-derived and arterial input functions for estimating the rate of glucose metabolism in therapy-monitoring 18F-FDG PET studies. *J Nucl Med*. 2006;47:945–9.
43. Chao S-L, Metens T, Lemort M. TumourMetrics: a comprehensive clinical solution for the standardization of DCE-MRI analysis in research and routine use. *Quant Imaging Med Surg*. 2017;7:496–510.
44. Billett HH. Hemoglobin and Hematocrit. In: Walker HK, Hall WD, Hurst JW, editors. *Clinical methods: the history, physical, and laboratory examinations* [Internet]. 3rd ed. Boston: Butterworths; 1990 [cited 2020 Feb 23]. Available from: <http://www.ncbi.nlm.nih.gov/books/NBK259/>.
45. Shen Y, Goerner FL, Snyder C, Morelli JN, Hao D, Hu D, et al. T1 relaxivities of gadolinium-based magnetic resonance contrast agents in human whole blood at 1.5, 3, and 7 T: Investigative. *Radiology*. 2015;50:330–8.
46. Tofts PS. Modeling tracer kinetics in dynamic Gd-DTPA MR imaging. *J Magn Reson Imaging*. 1997;7:91–101.
47. Schober P, Boer C, Schwarte LA. Correlation coefficients: appropriate use and interpretation. *Anesth Analg*. 2018;126:1763–8.
48. Ushijima K, Tsukamoto S, Yamazaki K, Yoshino I, Sugio K, Sugimachi K. High vascularity in the peripheral region of non-small cell lung cancer tissue is associated with tumor progression. *Lung Cancer*. 2001;34:233–41.
49. Birau A, Ceausu RA, Cimpean AM, Gaje P, Raica M, Olariu T. Assessment of angiogenesis reveals blood vessel heterogeneity in lung carcinoma. *Oncol Lett*. 2012;4:1183–6.
50. Silvestri E, Scolozzi V, Rizzo G, Indovina L, Castellaro M, Mattoli MV, et al. The kinetics of 18F-FDG in lung cancer: compartmental models and voxel analysis. *EJNMMI Res*. 2018;8:88.
51. Simoncic U, Leibfarth S, Welz S, Schwenzer N, Schmidt H, Reischl G, et al. Comparison of DCE-MRI kinetic parameters and FMISO-PET uptake parameters in head and neck cancer patients. *Med Phys*. 2017;44:2358–68.
52. Lee KH, Kang SK, Goo JM, Lee JS, Cheon GJ, Seo S, et al. Relationship between Ktrans and K1 with simultaneous versus separate MR/PET in rabbits with VX2 tumors. *Anticancer Res*. 2017;37:1139–48.
53. Mullani NA, Herbst RS, O'Neil RG, Gould KL, Barron BJ, Abbruzzese JL. Tumor blood flow measured by PET dynamic imaging of first-pass 18F-FDG uptake: a comparison with 15O-labeled water-measured blood flow. *J Nucl Med*. 2008;49:517–23.
54. Sourbron SP, Buckley DL. On the scope and interpretation of the Tofts models for DCE-MRI. *Magn Reson Med*. 2011;66:735–45.
55. Tofts PS, Brix G, Buckley DL, Evelhoch JL, Henderson E, Knopp MV, et al. Estimating kinetic parameters from dynamic contrast-enhanced T1-weighted MRI of a diffusible tracer: standardized quantities and symbols. *J Magn Reson Imaging*. 1999;10:223–32.
56. Lavini C. Simulating the effect of input errors on the accuracy of Tofts' pharmacokinetic model parameters. *Magn Reson Imaging*. 2015;33:222–35.
57. Kim H. Variability in quantitative DCE-MRI: sources and solutions. *J Nat Sci*. 2018;4.
58. Shukla-Dave A, Obuchowski NA, Chenevert TL, Jambawalikar S, Schwartz LH, Malyarenko D, et al. Quantitative imaging biomarkers alliance (QIBA) recommendations for improved precision of DWI and DCE-MRI derived biomarkers in multicenter oncology trials: QIBA Recommendations. *Journal of Magnetic Resonance Imaging* [Internet]. 2018 [cited 2019 May 28]; Available from: <http://doi.wiley.com/10.1002/jmri.26518>.
59. Heye T, Davenport MS, Horvath JJ, Feuerlein S, Breault SR, Bashir MR, et al. Reproducibility of dynamic contrast-enhanced MR imaging. Part I. Perfusion characteristics in the female pelvis by using multiple computer-aided diagnosis perfusion analysis solutions. *Radiology*. 2013;266:801–11.
60. Filipovic M, Vuissoz P-A, Codreanu A, Claudon M, Felbinger J. Motion compensated generalized reconstruction for free-breathing dynamic contrast-enhanced MRI. *Magn Reson Med*. 2011;65:812–22.

61. Spence AM, Muzi M, Graham MM, O'Sullivan F, Krohn KA, Link JM, et al. Glucose metabolism in human malignant gliomas measured quantitatively with PET, 1-[C-11]glucose and FDG: analysis of the FDG lumped constant. *J Nucl Med*. 1998;39:440–8.
62. Doot RK, Dunnwald LK, Schubert EK, Muzi M, Peterson LM, Kinahan PE, et al. Dynamic and static approaches to quantifying 18F-FDG uptake for measuring cancer response to therapy, including the effect of granulocyte CSF. *J Nucl Med*. 2007;48:920–5.
63. Yuan X, Zhang J, Quan C, Cao J, Ao G, Tian Y, et al. Differentiation of malignant and benign pulmonary nodules with first-pass dual-input perfusion CT. *Eur Radiol*. 2013;23:2469–74.
64. Li XS, Fan HX, Fang H, Huang H, Song YL, Zhou CW. Value of whole-tumor dual-input perfusion CT in predicting the effect of multiarterial infusion chemotherapy on advanced non-small cell lung cancer. *Am J Roentgenol*. 2014;203:W497–505.
65. Nguyen-Kim TDL, Frauenfelder T, Strobel K, Veit-Haibach P, Huellner MW. Assessment of bronchial and pulmonary blood supply in non-small cell lung cancer subtypes using computed tomography perfusion: Investigative. *Radiology*. 2015;50:179–86.
66. Ohno Y, Koyama H, Fujisawa Y, Yoshikawa T, Seki S, Sugihara N, et al. Dynamic contrast-enhanced perfusion area detector CT for non-small cell lung cancer patients: influence of mathematical models on early prediction capabilities for treatment response and recurrence after chemoradiotherapy. *Eur J Radiol*. 2016;85:176–86.
67. Lee SH, Rimner A, Deasy JO, Hunt MA, Tyagi N. Dual-input tracer kinetic modeling of dynamic contrast-enhanced MRI in thoracic malignancies. *J Appl Clin Med Phys*. 2019;20:169–88.
68. Milne EN. Circulation of primary and metastatic pulmonary neoplasms. A postmortem microarteriographic study. *Am J Roentgenol Radium Therapy, Nucl Med*. 1967;100:603–19.
69. Duan C, Kallehauge JF, Bretthorst GL, Tanderup K, Ackerman JJH, Garbow JR. Are complex DCE-MRI models supported by clinical data? *Magn Reson Med*. 2017;77:1329–39.
70. Leach MO, Brindle KM, Evelhoch JL, Griffiths JR, Horsman MR, Jackson A, et al. The assessment of antiangiogenic and antivascular therapies in early-stage clinical trials using magnetic resonance imaging: issues and recommendations. *Br J Cancer*. 2005;92:1599–610.
71. O'Connor JP, Jackson A, Asselin M-C, Buckley DL, Parker GJ, Jayson GC. Quantitative imaging biomarkers in the clinical development of targeted therapeutics: current and future perspectives. *The Lancet Oncology*. 2008;9:766–76.
72. Kelly RJ, Rajan A, Force J, Lopez-Chavez A, Keen C, Cao L, et al. Evaluation of KRAS mutations, angiogenic biomarkers, and DCE-MRI in patients with advanced non-small-cell lung cancer receiving sorafenib. *Clin Cancer Res*. 2011;17:1190–9.
73. Besson FL, La Joie R, Doeuvre L, Gaubert M, Mezenge F, Egret S, et al. Cognitive and brain profiles associated with current neuroimaging biomarkers of preclinical Alzheimer's disease. *J Neurosci*. 2015;35:10402–11.

Publisher's Note

Springer Nature remains neutral with regard to jurisdictional claims in published maps and institutional affiliations.

Submit your manuscript to a SpringerOpen[®] journal and benefit from:

- Convenient online submission
- Rigorous peer review
- Open access: articles freely available online
- High visibility within the field
- Retaining the copyright to your article

Submit your next manuscript at ► [springeropen.com](https://www.springeropen.com)
